

Optical conductivity of bilayer graphene with and without an asymmetry gap

E.J. Nicol

*Department of Physics, University of Guelph, Guelph, Ontario, N1G 2W1, Canada**

J.P. Carbotte

Department of Physics and Astronomy, McMaster University, Hamilton, Ontario, L8S 4M1, Canada

(Dated: October 23, 2018)

When a bilayer of graphene is placed in a suitably configured field effect device, an asymmetry gap can be generated and the carrier concentration made different in each layer. This provides a tunable semiconducting gap, and the valence and the conduction band no longer meet at the two Dirac points of the graphene Brillouin zone. We calculate the optical conductivity of such a semiconductor with particular emphasis on the optical spectral weight redistribution brought about by changes in gap and chemical potential due to charging. We derive an algebraic formula for arbitrary value of the chemical potential for the case of the bilayer conductivity without a gap.

PACS numbers: 78.67.-n, 78.20.Ci, 78.67.Pt, 81.05.Uw

I. INTRODUCTION

Graphene is known to exhibit special properties related to the Dirac nature of its quasiparticle dynamics. As an example, a half-integer quantum Hall effect is observed^{1,2} as was predicted^{3,4}. Bilayer graphene also possesses remarkable properties. When placed in a suitably configured field effect device, a tunable semiconducting gap can be generated with the result that the valence and the conduction band no longer meet at the two Dirac points in the graphene Brillouin zone^{5,6,7,8,9}. For a review of other remarkable properties of such systems as well as a discussion of possible technological applications, the reader is referred to Ref.^{10,11}. The optical conductivity of a few-layer epitaxial graphite^{12,13} and oriented pyrolytic graphite^{14,15} in finite external magnetic field has been reported recently, as well as for graphene¹⁶. There have also been theoretical studies^{9,17,18,19,20} of the conductivity, including discussions of optical sum rules^{21,22} which continue to provide useful information²³ on the electron dynamics. In Ref.²² it was found that the opening of the asymmetry gap in bilayer graphene leads to very small changes in the overall optical sum. Here we consider the optical conductivity of such a system with particular emphasis on the optical spectral weight redistribution brought about by changes in the chemical potential, due to charging, and to the opening of a semiconducting gap. In the configuration envisioned here, donor atoms are seeded on the upper face of a bilayer which is also placed in a field effect device so that the carrier imbalance in each layer is different as is the electrostatic potential.

The structure of our paper is organized as follows. In section II, we outline the theoretical derivation of the optical conductivity starting from the simplest nearest-neighbor tight-binding Hamiltonian which includes terms associated with the biased bilayer configuration. In section III, we present results for the case without the anisotropy gap, pertinent to the unbiased graphene bilayer. Here, we have been able to derive a surprisingly simple analytical formula for the frequency-dependent

conductivity for arbitrary choice of chemical potential and we have tested it against the full numerical solution and find good agreement, making this a very useful formula for experimentalists. In pure monolayer graphene, the conductivity is flat for the half-filled case of $\mu = 0$ and has a universal value of $\pi e^2/2h$. With finite μ , the spectral weight below a frequency $\Omega = 2\mu$ is transferred to a Drude metallic response at zero frequency.²⁴ We find in the case of the pure bilayer, for the half-filled $\mu = 0$ case, the conductivity retains a universal value at $\omega = 0$ and at high frequency, which is now twice the monolayer case, i.e. $\pi e^2/h$. Structure in the conductivity is found at $\Omega = \gamma$ and 2γ , with the structure at γ being particularly pronounced due to a doubly degenerate set of interband transitions. With finite μ , the doubly degenerate set of transitions is split into two separate features and a new strong absorption at γ is seen due to the nesting of two energy bands. At low energy, spectral weight is once again removed below 2μ and a Drude peak occurs. In section IV, we consider the case of the bilayer with an asymmetry gap. The main results in this case is the appearance of a semiconducting gap in the conductivity for $\mu = 0$ and a shift in the structure of the doubly degenerate interband transitions to higher energy. For finite μ , the metallic behavior is restored and a Drude peak occurs accompanied by loss of spectral weight below 2μ and the structure due to the doubly degenerate transitions is split, as before. The nesting feature at γ in the unbiased bilayer is now shifted to a new value and is broadened due to imperfect nesting of the energy bands. Finally, we end our analysis with a discussion in Section V.

II. THEORETICAL BACKGROUND

In order to derive and discuss the optical conductivity of biased bilayer graphene, we need to examine the form of the band structure and provide an expression for the electronic Green's function. To this end, we begin with

the Hamiltonian for the system under consideration and follow the notation given by McCann⁷ and Benfatto et

al.²² for continuity. The single spin Hamiltonian is given as:

$$\begin{aligned}
 H = & -t \sum_{\mathbf{n}, \boldsymbol{\delta}} (a_{1\mathbf{n}+\boldsymbol{\delta}}^\dagger b_{1\mathbf{n}} + h.c.) - t \sum_{\mathbf{n}, \boldsymbol{\delta}'} (a_{2\mathbf{n}}^\dagger b_{2\mathbf{n}+\boldsymbol{\delta}'} + h.c.) + \gamma \sum_{\mathbf{n}} (a_{2\mathbf{n}}^\dagger b_{1\mathbf{n}} + h.c.) \\
 & - \frac{1}{2} \Delta \sum_{\mathbf{n}} (a_{1\mathbf{n}+\boldsymbol{\delta}_1}^\dagger a_{1\mathbf{n}+\boldsymbol{\delta}_1} + b_{1\mathbf{n}}^\dagger b_{1\mathbf{n}}) + \frac{1}{2} \Delta \sum_{\mathbf{n}} (a_{2\mathbf{n}}^\dagger a_{2\mathbf{n}} + b_{2\mathbf{n}+\boldsymbol{\delta}_1'}^\dagger b_{2\mathbf{n}+\boldsymbol{\delta}_1'}).
 \end{aligned} \tag{1}$$

The first two terms are the nearest neighbor hopping terms for electrons to move in each of the graphene planes, separately. The two planes are indexed by 1 and 2, with a single graphene sheet having two inequivalent atoms labelled *A* and *B*, as the arrangement of carbon atoms on the two-dimensional honeycomb lattice provides for two atoms per unit cell. The operator $b_{1\mathbf{n}}$ annihilates an electron on the *B*-atom site with site label \mathbf{n} in the graphene sheet with label 1 and $a_{1\mathbf{n}+\boldsymbol{\delta}}^\dagger$ creates an electron on the neighboring *A*-atom site in the same sheet positioned at $\mathbf{n} + \boldsymbol{\delta}$, where $\boldsymbol{\delta}$ can be one of three vectors which point to the three possible nearest neighbors. These vectors are enumerated as $\boldsymbol{\delta}_1 = -(\mathbf{a}_1 + \mathbf{a}_2)/3$, $\boldsymbol{\delta}_2 = (2\mathbf{a}_1 - \mathbf{a}_2)/3$, and $\boldsymbol{\delta}_3 = -(\mathbf{a}_1 - 2\mathbf{a}_2)/3$, where $\mathbf{a}_1 = (a\sqrt{3}/2, a/2)$ and $\mathbf{a}_2 = (a\sqrt{3}/2, -a/2)$ are the unit vectors of the triangular sublattice for the *A* or *B* atoms, and $a = |\mathbf{a}_1| = |\mathbf{a}_2| = \sqrt{3}a_{CC}$ with a_{CC} the distance between two nearest carbon atoms. Now in layering graphene sheets, there are several choices for stacking. The one under consideration here and in experiment, is that of the Bernal-type stacking where if the atoms are labelled *A1* and *B1* in sheet 1 and *A2* and *B2* in sheet 2, then the *A2* atoms are stacked directly over the *B1* atoms, but the *B2* atoms are stacked over the centers of the *A1-B1* carbon rings. Pictures of this structure can be found in several references^{8,11} and so we do not reproduce this here. Note, however, that if we use the index \mathbf{n} to reference the *B1* atoms, then transferring this index to the *A2* atoms directly above gives rise to indexing the nearest neighbor vectors in the second sheet relative to the *A* atoms and hence the vectors are orientated differently and labelled as $\boldsymbol{\delta}'_i = -\boldsymbol{\delta}_i$. This stacking means that in terms of nearest neighbors associated with interlayer coupling, the *A2* atom is the nearest neighbour of the *B1* atom through a direct vertical bond. Thus, in the Hamiltonian of Eq. (1), the third term shows the hopping term for an electron on the *B1* site to hop to the *A2* site in plane 2. The hopping parameter is given as γ and is typically about 0.4 eV. There is also a possibility to hop from *B1* to *B2* or *A1* to *A2* but these hopping energies are very small (see Ref.⁸ and references therein). Hopping from *A1* to *B2* in the Hamiltonian is another possibility and its energy is larger at ~ 0.315 eV,⁸ however, we do not display it in the Hamiltonian as we drop

this term to focus on the physics and results which come from the main interlayer coupling, the γ term, which is essential to the discussion of the bilayer configuration. Furthermore, we are considering a biased bilayer structure which can give rise to the very novel physics of being able to tune the bilayer from metallic to semiconducting behavior, consequently the biasing is indicated in Eq. (1) as a lowering of the energy on graphene plane 1 by an amount $\Delta/2$ and the raising of the energy on plane 2 by the same amount. This results in the last two terms of Eq. (1). The quantity Δ is referred to as the asymmetry gap. The Hamiltonian transforms in the standard way²⁵ to *k*-space and can be written as a matrix:

$$\hat{H} = \begin{pmatrix} -\frac{\Delta}{2} & 0 & 0 & \phi^*(\mathbf{k}) \\ 0 & \frac{\Delta}{2} & \phi(\mathbf{k}) & 0 \\ 0 & \phi^*(\mathbf{k}) & \frac{\Delta}{2} & \gamma \\ \phi(\mathbf{k}) & 0 & \gamma & -\frac{\Delta}{2} \end{pmatrix}, \tag{2}$$

where $\phi(\mathbf{k}) = -t \sum_{\boldsymbol{\delta}} e^{i\mathbf{k} \cdot \boldsymbol{\delta}} = -t \sum_{\boldsymbol{\delta}'} e^{-i\mathbf{k} \cdot \boldsymbol{\delta}'}$ and we have followed the notation of McCann⁷ by using an eigenvector $\Psi = (a_{1\mathbf{k}}, b_{2\mathbf{k}}, a_{2\mathbf{k}}, b_{1\mathbf{k}})$. The energy eigenvalues of this matrix define the band structure. As the bilayer has four atoms per unit cell (doubling that of single layer graphene), there are now four bands and these are given by:

$$\begin{aligned}
 \epsilon_\alpha^2(\mathbf{k}) &= \frac{\gamma^2}{2} + \frac{\Delta^2}{4} + |\phi(\mathbf{k})|^2 + (-1)^\alpha \Gamma, \\
 \Gamma &= \sqrt{\frac{\gamma^4}{4} + |\phi(\mathbf{k})|^2(\gamma^2 + \Delta^2)},
 \end{aligned} \tag{3}$$

where $\alpha = 1, 2$. Of these four bands, the lower energy ones $\pm\epsilon_1(\mathbf{k})$ are essentially the original graphene bands with low energy modification and the $\pm\epsilon_2(\mathbf{k})$ are higher energy bands reflecting the dimerized bond between *B1* and *A2*, which has an energy scale of γ . As the main low energy physics occurs at the two inequivalent *K* and *K'* points of the graphene Brillouin zone, the function $\phi(\mathbf{k})$ can be expanded around the *K* point in the continuum approximation (i.e., the limit of small lattice constant *a*) to be $|\phi(\mathbf{k})| \approx \hbar v_F \mathbf{k}$, where $v_F = \sqrt{3}ta/(2\hbar)$. With this approximation, if $\Delta = 0$ and $\gamma = 0$, we would recover the famous graphene band structure where $\epsilon = \pm \hbar v_F \mathbf{k}$ is the form of the dispersion around the so-called Dirac

points, which are two-fold degenerate for the uncoupled bilayer. However, if $\Delta = 0$ and $\gamma \neq 0$, the band structure around these points is modified to be quadratic in k (although still linear at larger k) and the degeneracy is lifted such that the dimerized bands are shifted by γ , as can be seen later on in our first figure. The presence of the bias energy Δ , produces an energy gap in the band structure and a “mexican hat” structure occurs in the lower energy band ϵ_1 with a minimum at $E_{g1} = \gamma\Delta/(2\sqrt{\gamma^2 + \Delta^2})$ at $|\phi(\mathbf{k})| = \phi(k_0) = \hbar v_F k_0$, where $k_0 = (\Delta/2)\sqrt{(\Delta^2 + 2\gamma^2)/(\Delta^2 + \gamma^2)}$ and a “hat” maximum at $E_{01} = \Delta/2$ for $k = 0$. This will be discussed further in Section IV. This unusual band structure and the presence of the energy scales of γ and Δ , gives rise to very rich structure in the frequency-dependent conductivity, as we will see.

With this Hamiltonian, it is straightforward to obtain the Green’s function \hat{G} through $\hat{G}^{-1} = z\hat{I} - \hat{H}$ or

$$\hat{G}^{-1}(z) = \begin{pmatrix} z + \frac{\Delta}{2} & 0 & 0 & -\phi^*(\mathbf{k}) \\ 0 & z - \frac{\Delta}{2} & -\phi(\mathbf{k}) & 0 \\ 0 & -\phi^*(\mathbf{k}) & z - \frac{\Delta}{2} & -\gamma \\ -\phi(\mathbf{k}) & 0 & -\gamma & z + \frac{\Delta}{2} \end{pmatrix}, \quad (4)$$

where $z = i\omega_n$, with $\omega_n = \pi T(2n + 1)$ the fermionic Matsubara frequency for $n = 0, \pm 1, \pm 2, \dots$ and T , the temperature. For our calculation of the optical conductivity, only certain elements of the Green’s function enter our final expression and they are: G_{11} , G_{22} , G_{33} , G_{44} , G_{13} , G_{24} . As $G_{22}(\Delta) = G_{11}(-\Delta)$, $G_{33}(\Delta) = G_{44}(-\Delta)$, and $G_{24}(\Delta, \phi) = G_{13}(-\Delta, \phi^*)$, it is sufficient to show only three elements explicitly:

$$G_{11} = \frac{(\Delta - 2z)(\Delta^2 + 4\gamma^2 - 4z^2) - 4|\phi(\mathbf{k})|^2(\Delta + 2z)}{8(z^2 - \epsilon_1^2)(z^2 - \epsilon_2^2)} \quad (5)$$

$$G_{44} = \frac{(\Delta + 2z)[(\Delta - 2z)^2 - 4|\phi(\mathbf{k})|^2]}{8(z^2 - \epsilon_1^2)(z^2 - \epsilon_2^2)}, \quad (6)$$

$$G_{13} = \frac{(2z - \Delta)\gamma\phi(\mathbf{k})}{2(z^2 - \epsilon_1^2)(z^2 - \epsilon_2^2)}. \quad (7)$$

The finite frequency conductivity is calculated through the standard procedure of using the Kubo formula²⁵. The real part of the conductivity is written in terms of the retarded current-current correlation function $\Pi_{\alpha\beta}(\Omega + i0^+)$ as

$$\sigma_{\alpha\beta}(\Omega) = \frac{\text{Im}\Pi_{\alpha\beta}(\Omega + i0^+)}{\Omega}, \quad (8)$$

where α and β indicate the spatial components (here we will be interested in the longitudinal conductivity parallel to the graphene sheets, σ_{xx}). The retarded current-current correlation function is also referred to as the polarization function which we calculate in Matsubara for-

malism as outlined by Mahan²⁵ and given as

$$\Pi_{\alpha\beta}(i\nu_m) = - \int_0^{1/T} d\tau e^{i\nu_m\tau} \langle T_\tau J_\alpha(\tau) J_\beta(0) \rangle, \quad (9)$$

where τ is imaginary time, T_τ is the time ordering operator and ν_m is the bosonic Matsubara frequency $2\pi mT$ for $m = 0, \pm 1, \pm 2, \dots$ and temperature T . In Eq. (8) $\Pi_{\alpha\beta}(\Omega + i0^+)$ is the analytic continuation of Eq. (9) to the real axis via $i\nu_m \rightarrow \Omega + i0^+$. The current operator is the sum over sites of the site-specific paramagnetic current operator²¹:

$$J_\alpha(\tau) = \sum_{\mathbf{n}} j_\alpha^P(\tau, \mathbf{n}). \quad (10)$$

In order to evaluate this, we require the particular current operator corresponding to our Hamiltonian. This is found via a Peierls substitution on Eq. (1), where the operators associated with hopping to a new site are modified as $a_{1\mathbf{n}+\delta}^\dagger b_{1\mathbf{n}} \rightarrow a_{1\mathbf{n}+\delta}^\dagger \exp(-\frac{ie}{\hbar} \int_{\mathbf{n}}^{\mathbf{n}+\delta} \mathbf{A} \cdot \mathbf{r}) b_{1\mathbf{n}}$. (Note that we have taken the velocity of light $c = 1$.) The new Hamiltonian with the vector potential \mathbf{A} is then expanded for small \mathbf{A} to first order and the paramagnetic current operator is given by $j_\alpha^P(\mathbf{n}) = -\partial H / \partial (A_\alpha(\mathbf{n}))$. For our Hamiltonian and the case of considering only currents in the graphene sheets, the paramagnetic current is given as

$$j_\alpha^P(\mathbf{n}) = -\frac{ite}{\hbar} \sum_{\delta} (\delta)_\alpha (a_{1\mathbf{n}+\delta}^\dagger b_{1\mathbf{n}} - h.c.) + \frac{ite}{\hbar} \sum_{\delta'} (\delta')_\alpha (a_{2\mathbf{n}}^\dagger b_{2\mathbf{n}+\delta'} - h.c.). \quad (11)$$

Note that the Hermitian conjugate piece has a minus sign representing a depletion of the current for hopping in the reverse direction. Fourier transforming to k -space and summing over \mathbf{n} , we can write the total paramagnetic current operator $J_\alpha(\mathbf{k}) = -e \sum_{\mathbf{k}} \Psi^\dagger \hat{v}_\alpha \Psi$, where

$$\hat{v}_\alpha = \begin{pmatrix} 0 & 0 & 0 & v_{\alpha\mathbf{k}}^* \\ 0 & 0 & v_{\alpha\mathbf{k}} & 0 \\ 0 & v_{\alpha\mathbf{k}}^* & 0 & 0 \\ v_{\alpha\mathbf{k}} & 0 & 0 & 0 \end{pmatrix}, \quad (12)$$

with $v_{\alpha\mathbf{k}} = -(it/\hbar) \sum_{\delta} (\delta)_\alpha e^{i\mathbf{k} \cdot \delta}$. The structure of the equation embodies the form of $j = -nev$ where the velocity v is proportional to the gradient of the energy. One can see that the factors of it and the sum over components of δ weighted by $e^{i\mathbf{k} \cdot \delta}$ are simply a result of taking the gradient of $\phi(\mathbf{k})$ which is the bare energy in the absence of Δ and γ , i. e., $v_{\mathbf{k}} = \nabla \phi(\mathbf{k})/\hbar$. Consequently, the polarization function can then be written in the usual bubble approximation as

$$\Pi_{\alpha\beta}(i\nu_m) = e^2 T \sum_{i\omega_n} \int \frac{d^2 k}{(2\pi)^2} \text{Tr}[\hat{v}_\alpha \hat{G}(i\omega_n + i\nu_m, \mathbf{k}) \hat{v}_\beta \hat{G}(i\omega_n, \mathbf{k})] \quad (13)$$

or, favoring the spectral function representation of the Green's function where

$$G_{ij}(z) = \int_{-\infty}^{\infty} \frac{d\omega}{2\pi} \frac{A_{ij}(\omega')}{z - \omega'}, \quad (14)$$

we can write the real part of the conductivity as

$$\sigma_{\alpha\beta}(\Omega) = \frac{e^2}{2\Omega} \int_{-\infty}^{\infty} \frac{d\omega}{2\pi} [f(\omega - \mu) - f(\omega + \Omega - \mu)] \int \frac{d^2 k}{(2\pi)^2} \text{Tr}[\hat{v}_\alpha \hat{A}(\omega + \Omega, \mathbf{k}) \hat{v}_\beta \hat{A}(\omega, \mathbf{k})], \quad (15)$$

where $f(x) = 1/[\exp(x/T) + 1]$ is the Fermi function and μ is the chemical potential. In presenting our results, we evaluate this equation at $T=0$. Taking the trace and dropping those terms which vanish in the averaging over

momentum, the structure of the equation to be evaluated reduces to knowing the three spectral functions associated with the three Green's functions mentioned earlier. The longitudinal conductivity $\sigma_{xx}(\omega) \equiv \sigma(\Omega)$ becomes

$$\begin{aligned} \sigma(\Omega) = & \frac{N_f e^2}{2\Omega} \int_{-\infty}^{\infty} \frac{d\omega}{2\pi} [f(\omega - \mu) - f(\omega + \Omega - \mu)] \int \frac{d^2 k}{(2\pi)^2} |v_{\mathbf{k}}|^2 \{ A_{11}(\omega, \Delta) A_{44}(\omega + \Omega, \Delta) + A_{44}(\omega, \Delta) A_{11}(\omega + \Omega, \Delta) \\ & + A_{11}(\omega, -\Delta) A_{44}(\omega + \Omega, -\Delta) + A_{44}(\omega, -\Delta) A_{11}(\omega + \Omega, -\Delta) \\ & + 2[A_{13}(\omega, \Delta) A_{13}^*(\omega + \Omega, -\Delta) + A_{13}^*(\omega, -\Delta) A_{13}(\omega + \Omega, \Delta)] \}. \end{aligned} \quad (16)$$

We evaluate this in the continuum approximation around the K point of the graphene Brillouin zone, where $|v_{\mathbf{k}}|^2 = v_F^2$ and $|\phi(\mathbf{k})| = \hbar v_F k$ and the integral over k has a large upper cutoff typical of the large bandwidth. Thus, we introduce a factor $N_f = 4$ which comes from a sum over spin (not included explicitly up till now) and a sum over the two inequivalent K points (K and K') in the graphene Brillouin zone. Previous to Eq. (16), the integral over $d^2 k$ was to be taken over the Brillouin zone, but in Eq. (16) it is to be interpreted as over a single K point which would be a cone for the decoupled bilayer graphene. If we take the limit of this expression (Eq (16)) for $\gamma = \Delta = \mu = 0$, we find a constant as a function of frequency given as $\sigma_0 = e^2/2\hbar$, which is twice the result for single layer graphene²⁴. We will refer to this as the conductivity of the uncoupled graphene bilayer. Finally, for illustration, we write an example of the spectral functions here:

$$A_{13}(\omega, \Delta) = \sum_{\alpha=1,2} [a_{13}(\alpha, \Delta) \delta(\omega - \epsilon_\alpha) + a_{13}(\alpha, -\Delta) \delta(\omega + \epsilon_\alpha)], \quad (17)$$

where

$$a_{13}(\alpha, \Delta) = (-1)^\alpha \frac{\pi}{2} \frac{(2\epsilon_\alpha - \Delta) \gamma \phi(\mathbf{k})}{\epsilon_\alpha (\epsilon_2^2 - \epsilon_1^2)}. \quad (18)$$

The other spectral functions follow from the Green's functions in a similar manner. For numerical work, we write the delta functions in the spectral functions as Lorentzians with a broadening η , i.e., $\delta(x) = (\eta/\pi)/[x^2 + \eta^2]$. In the optical conductivity, this manifests itself as an effective transport scattering rate of $1/\tau_{imp} = 2\eta$ due to the convolution of two delta functions in the conductivity formula.

III. RESULTS WITHOUT ANISOTROPY GAP

At zero temperature, for the case of $\Delta = 0$, it is possible to derive a closed algebraic formula for the bilayer

conductivity. It has the form:

$$\begin{aligned} \frac{\sigma(\Omega)}{\sigma_0} = & \left[\frac{\Omega + 2\gamma}{2(\Omega + \gamma)} + \frac{\Omega - 2\gamma}{2(\Omega - \gamma)} \Theta(\Omega - 2\gamma) \right] \Theta(\Omega - 2\mu) \\ & + \frac{\gamma^2}{2\Omega^2} [\Theta(\Omega - 2\mu - \gamma) + \Theta(\Omega - 2\mu + \gamma)] \Theta(\Omega - \gamma) \\ & + a(\mu)\delta(\Omega) + b(\mu)\delta(\Omega - \gamma) \end{aligned} \quad (19)$$

with

$$a(\mu) = \frac{4\mu(\mu + \gamma)}{2\mu + \gamma} + \frac{4\mu(\mu - \gamma)}{2\mu - \gamma} \Theta(\mu - \gamma) \quad (20)$$

and

$$b(\mu) = \frac{\gamma}{2} \left[\ln \frac{2\mu + \gamma}{\gamma} - \ln \frac{2\mu - \gamma}{\gamma} \Theta(\mu - \gamma) \right] \quad (21)$$

where $\sigma_0 = e^2/2\hbar$ which is twice the conductivity of a single graphene sheet. This expression correctly reduces to the form given by Abergel and Fal'ko¹⁸ in the limit of $\mu = 0$. In the top frame of Fig. 1, we show results for $\sigma(\Omega)/\sigma_0$ as a function of Ω/γ for the original Abergel and Fal'ko case of $\mu = 0$ (blue dashed curve), thus reproducing their results, and our extension to finite μ , specifically $\mu = 0.2\gamma$ (solid red curve) and $\mu = 1.2\gamma$ (dash-dotted blue). In the two last cases, the two delta functions at $\Omega = 0$ and $\Omega = \gamma$ are shown as vertical arrows. Their weight is given by $a(\mu)/2$ and $b(\mu)$ of Eqs. (20) and (21), respectively. Note, that only half of the delta function at $\Omega = 0$ is to be associated with the optical spectral weight for $\Omega \geq 0$. The arrows in Fig. 1a are shown schematically to represent their relative weight. The quantities $a(\mu)/2$ and $b(\mu)$ are shown in Fig. 2 as the long-dashed blue and short-dashed red curves, respectively, as a function of chemical potential μ normalized to the plane-to-plane hopping γ . Also, shown for comparison is the case of the uncoupled graphene bilayer with $\gamma = 0$ but μ finite (solid black curve). We see that the amount of spectral weight in the Drude delta function centered at $\Omega = 0$ is less than it is for pure graphene, except in the limit of $\mu \rightarrow 0$, when they are equal.

Besides the two delta functions, the finite μ result has regions of optical spectral weight lost when compared with the $\mu = 0$ case. In the solid red curve of Fig. 1 (top frame), the region from 0 to 2μ is completely depleted while a second region of partial depletion is seen above $\Omega = \gamma$. The optical spectral weight lost below 2μ , relative to the $\mu = 0$ finite gamma case, can easily be computed from Eq. (19) and is $c(\mu) \equiv \mu + (\gamma/2) \ln[(2\mu + \gamma)/\gamma]$, which is shown as the dash-dotted green curve in Fig. 2. For finite μ ($\mu < \gamma$), $c(\mu) > a(\mu)/2$ so that part of the lost spectral weight has been transferred to the second delta function at $\Omega = \gamma$. The existence of the two regions of depletion just described is encoded in the theta functions of Eq. (19) and is easily understood in terms of the energy dispersion curve diagrams displayed in the middle and bottom frames of Fig. 1, where we show possible optical transitions. We start with the middle frame where

the chemical potential, shown as the horizontal dotted line, is set at $\mu = 0$. The transitions are vertical and all connect a filled valence band to empty conduction band states. From left to right, the arrows depict typical transitions for the four possible ways of connecting the four bands: from $-\epsilon_2 \rightarrow +\epsilon_1$ and $-\epsilon_1 \rightarrow +\epsilon_2$, which are both restricted to photon energies $\Omega > \gamma$, and $-\epsilon_1 \rightarrow +\epsilon_1$ and $-\epsilon_2 \rightarrow +\epsilon_2$, with the latter one restricted to $\Omega > 2\gamma$. The onsets of transitions at $\Omega = \gamma$ and 2γ are clearly seen in the dashed blue curve of the top frame of Fig. 1.

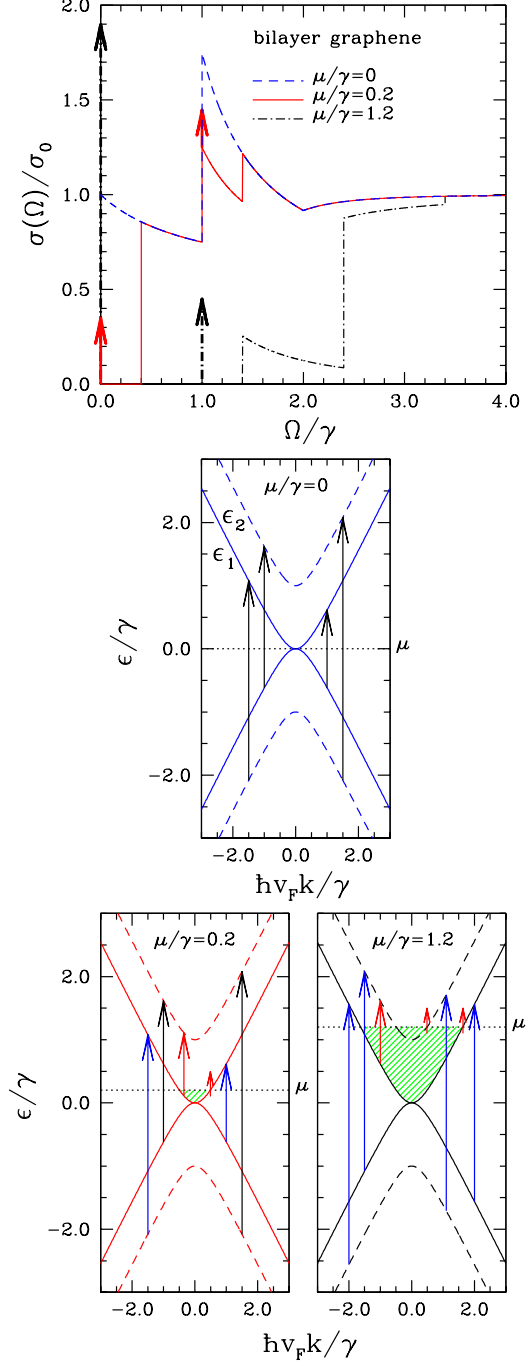
This is to be contrasted with the case of $\mu \neq 0$ shown in the lower frames. Starting again from the left, the first arrow describes transitions from $-\epsilon_2 \rightarrow +\epsilon_1$ as before but its color has been changed to blue to indicate that now there is a restriction that only transitions with $\Omega > \gamma + 2\mu$ are allowed. The next type of transition remains unchanged for $\mu < \gamma$, as is the case shown. However, new transitions shown as the red arrow from $+\epsilon_1 \rightarrow +\epsilon_2$, can now occur, which were not possible for $\mu = 0$. (The green shading represents the newly filled states due to finite μ which were formerly part of the empty conduction band.) Intraband transitions from $+\epsilon_1 \rightarrow +\epsilon_1$ are also possible and correspond to the delta function centered at $\Omega = 0$ which broadens to a Drude form when any kind of scattering is included. These transitions are depicted by a short red arrow with vanishing length for $\Omega \rightarrow 0$. The next set from $-\epsilon_1 \rightarrow +\epsilon_1$ are restricted to $\Omega > 2\mu$ while the last, $-\epsilon_2 \rightarrow +\epsilon_2$, remain unaltered. The spectral weight lost between 0 and 2μ and between γ and $\gamma + 2\mu$ is balanced by the appearance of the two delta function contributions originating from the two new transitions $+\epsilon_1 \rightarrow +\epsilon_2$ and $+\epsilon_1 \rightarrow +\epsilon_1$ (Drude). The first set of these transitions leads to a delta function at $\Omega = \gamma$ and this is traced to the perfect nesting of the bilayer dispersion curves for $\epsilon_1(\mathbf{k})$ and $\epsilon_2(\mathbf{k})$ which differ only by a constant displacement of γ . Should the electronic dispersions stop being nested due to, for example, higher neighbor hoppings, or as we will see, due to the opening of the semiconducting gap, the delta function will broaden into a “band”, the width of which is related to the mismatch of the dispersions from perfect nesting. In particular, as we have already stated, the hopping from A1 to B2 can be significant in size and will lead to changes in the band structure which are not cylindrically symmetric in the (k_x, k_y) -plane⁸. This fact complicates the mathematics and goes beyond the present work. However, the trigonal warping which arises can lead to subtle effects such as described by Mikitik and Sharlai²⁷ in relation to the Dirac points.

If $\mu > \gamma$, then further new transitions become possible. We now show an example for the case where $\mu = 1.2\gamma$ so that the $+\epsilon_2$ band is now partially occupied. The possible transitions are shown in the bottom righthand frame of Fig. 1. For the first time all the terms in Eq. (19) become activated. From the diagram $-\epsilon_2 \rightarrow +\epsilon_1$ transitions are restricted to $\Omega \geq 2\mu + \gamma$ (first term of second line in Eq. (19)) and the restriction on $-\epsilon_1 \rightarrow +\epsilon_2$ is $\Omega \geq 2(\mu - \gamma) + \gamma = 2\mu - \gamma$ (second term of second line in Eq. (19)).

FIG. 1: (Color online) Shown to the right. Upper frame: Frequency dependent conductivity $\sigma(\Omega)$ of the bilayer normalized to twice that of a single graphene sheet σ_0 versus Ω/γ for three values of the chemical potential, as indicated, and $\Delta = 0$. Middle frame: Dispersion of ϵ_1 (solid line) and ϵ_2 (dashed) of the bilayer near the K point with the bands split by γ , showing the four types of transitions possible when $\mu = 0$. Bottom frames: Transitions possible in the band structure for finite chemical potential of $\mu = 0.2\gamma$ (lefthand side) and 1.2γ (righthand side). See text for discussion.

Both the $-\epsilon_1 \rightarrow +\epsilon_1$ and $-\epsilon_2 \rightarrow +\epsilon_2$ arise only for $\Omega \geq 2\mu$ (first line of Eq. (19)) and new intraband transitions $+\epsilon_2 \rightarrow +\epsilon_2$ add the second term in $a(\mu)$. The $b(\mu)$ is depleted through an additional negative contribution for $\mu > \gamma$, because the $+\epsilon_1 \rightarrow +\epsilon_2$ nested transitions are partially blocked by the filled states in $+\epsilon_2$ near $k = 0$. These facts manifest themselves in the top frame of Fig. 1 as a large peak centered at $\Omega = 0$ and another at $\Omega = \gamma$ from $a(\mu)$ and $b(\mu)$, respectively. All other transitions are completely suppressed below $\Omega = 2\mu = 2.4\gamma$ except for a small contribution from $-\epsilon_1 \rightarrow +\epsilon_2$ clearly seen between $2\mu - \gamma = 1.4\gamma$ and 2.4γ . In addition, the added possible transitions above $2\mu + \gamma = 3.4\gamma$ are seen to provide a small additional jump in $\sigma(\Omega)$ at this energy.

In Fig. 3, we compare the results obtained on the basis of Eq. (19) with the numerical evaluation of the complete formula Eq. (16). For this evaluation a finite value for the electron scattering rate $1/\tau_{imp} = 2\eta$ is needed. We took it to be a constant in energy and equal to 0.04γ . This is the simplest of models and is sufficient for our purpose here. In general, the electron self-energy is a frequency-dependent complex function with non-vanishing real part. For impurity scattering, the detailed energy dependence of these functions will depend on the scattering potential and will be different for strong (unitary) and weak (Born) scattering as discussed at length in a recent preprint²⁶. The energy dependence of the scattering rate can lead to interesting effects as discussed by Gusynin et al.²¹ for the case of the microwave conductivity where a cusp-like behavior is predicted to arise instead of the Lorentzian-like dependence of the usual Drude form. Here, it is sufficient to use a constant scattering rate in which case the real part of the self-energy, which is Kramers-Kronig related, is zero. Returning to the comparison in Fig. 3, we note that for the analytic formula (19) we broadened out the delta functions into Lorentzians using $\delta(x) = (\Gamma/\pi)/(x^2 + \Gamma^2)$, where $\Gamma = 1/\tau_{imp} = 0.04\gamma$ to match the full numerical work. The agreement between the numerical calculation (solid red curve) and the results of formula (19) (dashed blue curve) is excellent. The differences arise solely because no scattering was included in the dashed blue curve beyond broadening the two delta function contributions at $\Omega = 0$ and $\Omega = \gamma$ for ease of comparison. We have verified that making $1/\tau_{imp}$ smaller brings the two curves closer, as it must. Note, that concurrent numerical work



to ours²⁶ shows the case of $2\mu = \gamma$ with varying impurity scattering. Their results agree with ours. Similar good agreement between our analytic results based on Eq. (19) and the full numerical evaluation of Eq. (16) is seen in the lower frame of Fig. 3 for $\mu = 1.2\gamma$. Indeed, we see that broadening the delta functions of the analytical formula, as we have done, is essential to capture the result that the optical absorption below $2\mu - \gamma$, in this case, is not zero but actually finite everywhere. This makes Eq. (19) a useful formula for experimentalists.

The issue of optical spectral weight redistribution with changes in chemical potential can be addressed in a more

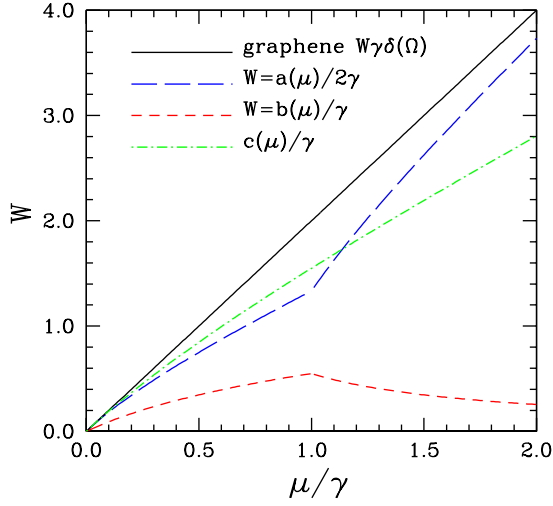


FIG. 2: (Color online) The evolution of the positive frequency spectral weight W , found under each of the delta functions in Eq. (19), as function of chemical potential. The case of an uncoupled graphene bilayer is given for comparison and the quantity $c(\mu)$ represents the spectral weight missing in the conductivity for $0 < \Omega < 2\mu$ relative to the $\mu = 0$ case.

global fashion than we have done so far by introducing the partial optical sum:

$$I(\Omega) = \int_{0+}^{\Omega} \frac{\sigma(\omega)}{\sigma_0} d\omega \quad (22)$$

defined as the area under the conductivity up to energy Ω . This is shown in Fig. 4 for five values of the chemical potential: $\mu/\gamma = 0$ (solid black), 0.3 (long-dashed green), 0.5 (short-dash-dotted red), 0.9 (long-dash-dotted pink) and 1.2 (short-dashed blue). In all cases by $\Omega/\gamma = 3$, the highest frequency shown, the integrated spectral weight has returned to its $\mu = 0$ value (solid black curve) and the introduction of a finite charge carrier imbalance has not changed the partial optical sum up to that energy, although it has significantly changed its distribution in energy in the range $0 < \Omega < 3\gamma$. Note in particular the sharp rise out of $\Omega = 0$ exhibited by all curves except for $\mu = 0$. This reflects the presence of the delta function contribution at $\Omega = 0$ which increases with increasing μ . The curves start to flatten when most of the spectral weight of the Drude contribution is integrated and consequently, this plateau occurs at about the same value as $a(\mu)$ plotted in Fig. 2. A second steep rise is also seen at $\Omega = \gamma$ due to the second delta function in Eq. (19). For the long-dashed green curve, we note the abrupt change in slope at $\Omega = 2\mu = 0.6\gamma$ which has moved to γ in the short-dash-dotted red curve, to 1.8γ in the long-dash-dotted pink curve and to 2.4γ in the short-dashed blue curve. These all reflect the 2μ cutoff. Note also in this last case, the small kink at $2\mu - \gamma$ which reflects the onset of the $-\epsilon_1 \rightarrow +\epsilon_2$ optical transitions.

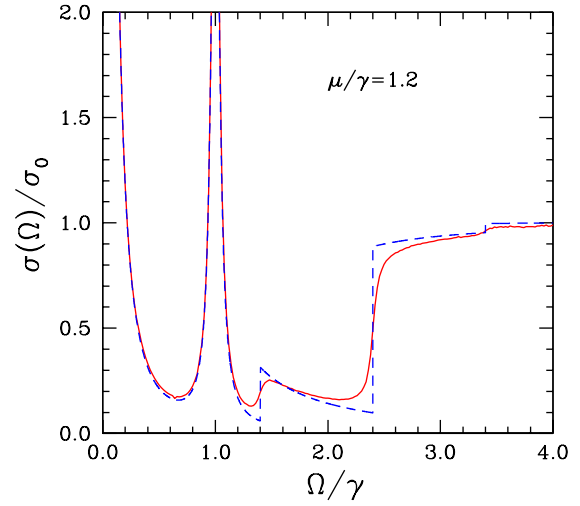
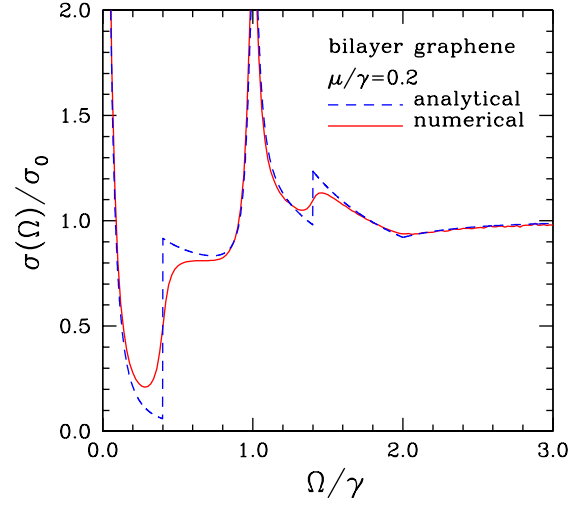


FIG. 3: (Color online) Comparison between the full numerical evaluation of the conductivity [Eq. (16)] and the analytical formula of Eq. (19). For Eq. (19) the delta functions are broadened into Lorentzians with a scattering rate to match the effective scattering rate in the numerical work. Two different regimes of μ are shown: $\mu = 0.2\gamma$ (upper frame) and 1.2γ (lower frame).

IV. RESULTS WITH ANISOTROPY GAP

For the finite gap case, we begin with a discussion of the important energy scales involved. In the top frame of Fig. 5, we show the dispersion curves for our two bands: ϵ_1 (solid red curves) and ϵ_2 (dashed blue curves). The first band shows a Mexican hat structure. For positive energies, there is a local maximum at zero momentum $\phi = \hbar v_F k = 0$ with $\epsilon_1 = \Delta/2 \equiv E_{01}$. There are also two minimum at finite $\phi = \pm(\Delta/2)\sqrt{(\Delta^2 + 2\gamma^2)/(\Delta^2 + \gamma^2)} \equiv \hbar v_F k_0$ with energy $\Delta\gamma/(2\sqrt{\Delta^2 + \gamma^2}) \equiv E_{g1}$. The lowest energy for which optical transitions are possible in the semiconducting case is $2E_{g1}$, when there is no charge

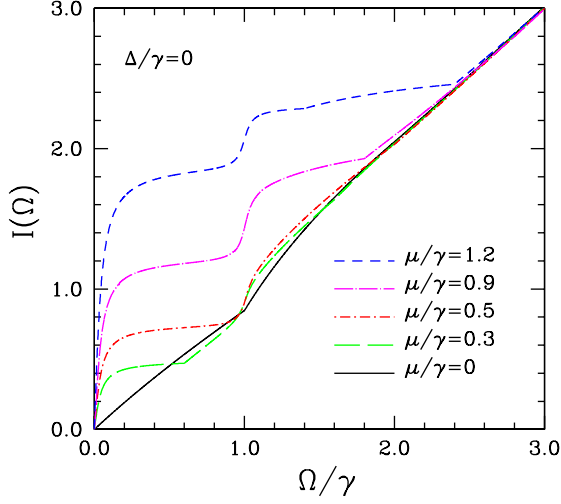


FIG. 4: (Color online) Partial optical sum $I(\Omega)$ in units of γ versus Ω/γ for various values of chemical potential, as indicated in the figure.

carrier imbalance which would introduce a finite μ . For understanding optical transitions, other energies are also significant and these are indicated in Fig. 5. At $k = 0$, $\epsilon_2(k = 0) = \sqrt{\gamma^2 + (\Delta/2)^2} \equiv E_{02}$ and at the momentum of the minimum in band 1, the energy in band 2

is $\epsilon_2(k_0) = \sqrt{(\Delta^4 + \gamma^4 + 9\Delta^2\gamma^2/4)/(\gamma^2 + \Delta^2)} \equiv E_{g2}$. In addition, when a finite value of chemical potential is considered with $\mu > \Delta\gamma/(2\sqrt{\Delta^2 + \gamma^2})$ as shown, two other energies are important, namely the energy ϵ_2 for momenta at which μ crosses the ϵ_1 dispersion curve. These are $\sqrt{\gamma^2 + \Delta^2 + \mu^2 + 2L} \equiv E_B$ and if $\mu < \Delta/2$, $\sqrt{\gamma^2 + \Delta^2 + \mu^2 - 2L} \equiv E_A$, where $L = \sqrt{\mu^2(\Delta^2 + \gamma^2) - (\gamma\Delta/2)^2}$. These quantities determine the onset of various processes as we will describe below and are entered in Table I. Before doing so, it is important to understand how the electronic density of states $N(\epsilon)$ varies with ϵ since its value at the initial and the final value of the energy for a given optical transition provides an important weighting factor for such processes.

In the general case, one can obtain an analytic algebraic expression for total double-spin $N(\epsilon)$ in terms of the partial density of states provided by band 1 and band 2, N_1 and N_2 , respectively,

$$N(\epsilon) = N_1(\epsilon) + N_2(\epsilon), \quad (23)$$

where

$$N_1(\epsilon) = [N_1^+(\epsilon) - N_1^-(\epsilon)\Theta(E_{01} - \epsilon)]\Theta(\epsilon - E_{g1}), \quad (24)$$

$$N_2(\epsilon) = N_2^-(\epsilon)\Theta(\epsilon - E_{02}), \quad (25)$$

with

$$N_\alpha^\pm(\epsilon) = \frac{2}{\pi\hbar^2 v_F^2} \frac{\epsilon}{1 + (-1)^\alpha (\gamma^2 + \Delta^2)/C},$$

$$C = \sqrt{\gamma^4 + (\gamma^2 + \Delta^2)[4\epsilon^2 + \Delta^2 \pm 2\sqrt{4\epsilon^2(\Delta^2 + \gamma^2) - \gamma^2\Delta^2}]}. \quad (26)$$

The two terms for N_1 simply reflect the two pieces of the energy dispersion for ϵ_1 : the large k piece and the small k piece associated with the mexican hat. The density of states normalized by $\gamma/\hbar^2 v_F^2$ is shown in the bottom frame of Fig. 5 for several values of Δ . The long-dashed green curve is for the uncoupled graphene bilayer with $\gamma = \Delta = 0$ and is included for comparison. We note that beyond $\epsilon/\gamma \sim 1.2$ for the parameters shown here, the various curves come close together on the scale of the figure. The inset show the density of states associated with each band separately for the case of $\Delta = 1.5\gamma$. The ϵ_1 dispersion gives rise to the square root singularity, followed by a shoulder, that is seen in the total density of states. Indeed the singularity in both the solid and short-dashed curves of the main frame at $\epsilon = E_{g1}$ and the shoulder at $\Delta/2$, have their origins in the mexican hat structure of the dispersion curve. The shoulder comes from the top of the hat and is a van Hove singularity associated with the dispersion flattening at this point. The square root

singularity can be derived for ϵ near the hat minimum $\epsilon \sim E_{g1}$ and we find, as others²⁶ have done,

$$N(\epsilon) = \frac{k_0}{4\pi\hbar} \sqrt{\frac{2m^*}{\epsilon - E_{g1}}}. \quad (27)$$

The factor $k_0 = (\Delta/2\hbar v_F)\sqrt{(\Delta^2 + 2\gamma^2)/(\Delta^2 + \gamma^2)}$, which is the momentum associated with the rim of the mexican hat, is related to the degeneracy of energies around the circular minimum of the mexican hat (fixed magnitude, varying angle of momentum) while the square root is associated with the one-dimensional variation in energy up and down the rim with varying magnitude of k (fixed angle), making this equivalent to what is expected for a one-dimensional density of states. The effective mass is $m^* = \frac{\gamma}{2\Delta v_F^2} \frac{[\Delta^2 + \gamma^2]^{3/2}}{\Delta^2 + 2\gamma^2}$ with energy $\epsilon = E_{g1} + \frac{\hbar^2}{2m^*}(k - k_0)^2$. For comparing with Eq. (23), it is

TABLE I: Energies involved in optical transitions (see top frame of Fig. 5) for the case $\gamma = 0.4$ eV, $\Delta = 0.6$ eV and two values of chemical potential $\mu = 0.25$ and 0.35 eV.

Energy	Formula	value in eV for $\mu = 0.25$ eV	value in eV for $\mu = 0.35$ eV
E_{g1}	$\gamma\Delta/(2\sqrt{\gamma^2 + \Delta^2})$	0.166	0.166
E_{g2}	$\sqrt{(\Delta^4 + \gamma^4 + 9\Delta^2\gamma^2/4)/(\gamma^2 + \Delta^2)}$	0.74	0.74
E_{01}	$\Delta/2$	0.3	0.3
E_{02}	$\sqrt{\gamma^2 + (\Delta/2)^2}$	0.5	0.5
E_A	$\sqrt{\gamma^2 + \Delta^2 + \mu^2 - 2L}$	0.56	-
E_B	$\sqrt{\gamma^2 + \Delta^2 + \mu^2 + 2L}$	0.92	1.042
where $L = \sqrt{\mu^2(\gamma^2 + \Delta^2) - (\gamma\Delta/2)^2}$			

convenient to rewrite Eq. (27) in the form:

$$N(\epsilon) = \frac{1}{8\pi\hbar^2 v_F^2} \sqrt{\frac{\gamma\Delta\sqrt{\Delta^2 + \gamma^2}}{\epsilon - E_{g1}}}. \quad (28)$$

This singularity plays an important role in optics because it leads to peaks in $\sigma(\Omega)$ when the energy of either or both the initial and final states involved falls at E_{g1} . This fact, plus the energy scales identified in Fig. 5 (top frame) allows one to understand the qualitative features of our numerical results for the conductivity.

Referring to Fig. 6, we start with the upper frame, where $\Delta = 0.2\gamma$. Three values of the chemical potential μ are considered. The dashed blue curve, which is for reference, has $\mu = 0$, the dash-dotted black is for $\mu = 0.1\gamma$ and the solid red is for $\mu = 0.2\gamma$. We begin with the dashed blue curve which is the only case which exhibits a true semiconducting gap with no absorption up to photon energy $\Omega = 2E_{g1} = 0.196\gamma$. We first note the existence of a small tail below this energy and also note that the main rise is smeared. This is because we have used a finite impurity scattering rate of $1/\tau_{imp} = 0.04\gamma$ in all of our numerical work. It is clear that most of the states lost below the gap ($2E_{g1}$) are to be found piled up in a region of order a few E_{g1} above it. Later we will examine in detail this optical spectral weight redistribution. This part of the curve for $\sigma(\Omega)$ is due to the $-\epsilon_1 \rightarrow +\epsilon_1$ transitions and their onset involves the singular density of states at E_{g1} for both initial and final states. The second peak in the dashed blue curve is traced to transitions $-\epsilon_2 \rightarrow +\epsilon_1$ and $-\epsilon_1 \rightarrow +\epsilon_2$ (degenerate in energies) and these involve a single singular $N(\epsilon)$ either in the initial or final state but not for both, and the onset is at $E_{02} + E_{01} = \sqrt{\gamma^2 + (\Delta/2)^2} + \Delta/2 \simeq 1.1\gamma$. It is also clear from Fig. 5 (top frame) that this onset remains even for finite μ because the $-\epsilon_1 \rightarrow +\epsilon_2$ transition is never blocked by a finite μ value provided μ falls below the minimum in ϵ_2 which is the case considered here.

Next we consider the dash-dotted black curve for $\mu = 0.1\gamma$. In this case, the $-\epsilon_1 \rightarrow +\epsilon_1$ transitions are no longer possible for energies less than or equal to $2\mu = 0.2\gamma$ because these states are occupied and cannot be used as final states in optical transitions. The energy $2\mu = 0.2\gamma$ is very close to the onset for the dashed blue

curve with $\mu = 0$ which is at 0.196γ and, as a result, both dashed and dash-dotted curves are close to each other in this energy region. Nevertheless it is important to understand that while the dashed blue curve is in principle encoded with the information on the details of the mexican hat topology, the dash-dotted black curve is less so as it involves, in addition, a sharp cut off at 0.2γ , which obscures some of these details. Finally we note the transfer of optical spectral weight to a Drude peak centered at $\Omega = 0$ due to $+\epsilon_1 \rightarrow +\epsilon_1$ intraband transitions. This peak does not exist at zero temperature for $\Delta \neq 0$ and $\mu = 0$.

The next interesting feature in the dash-dotted black curve is the peak slightly above $\Omega = 0.9\gamma$. This peak can be traced to new $+\epsilon_1 \rightarrow +\epsilon_2$ optical transitions made possible for finite μ . We have already seen that, for $\Delta = 0$, these would fall at $\Omega = \gamma$ and provide, in the clean limit, a delta function contribution which can be traced to the perfect nesting of the dispersion curves. But for finite Δ , perfect nesting no longer occurs and these transitions broaden into a “band” as well as shift in energy as we now describe. Returning to Fig. 5 (top frame), we note that because $+\epsilon_1$ states are now occupied in a region about the mexican hat minimum, transitions from $+\epsilon_1 \rightarrow +\epsilon_2$ become possible for photon energies between $E_A - \mu$ and $E_B - \mu$. The intermediate energy transition at $E_{g2} - E_{g1}$ involves the density of states at the bottom of the mexican hat and this is expected to lead to a peak in $\sigma(\Omega)$ at this energy. For the parameters of the model, the new “band” ranges in energy between 0.915γ to 0.934γ , with a peak at 0.93γ . In Fig. 6, an additional broadening of this narrow “band” is included because we have used a finite $1/\tau_{imp}$. Nevertheless, overall, the new “band” does not broaden much as a result of scattering and the changed topology of the energy dispersion curves $\epsilon_1(\mathbf{k})$ and $\epsilon_2(\mathbf{k})$. While the dispersion curves $+\epsilon_1$ and $+\epsilon_2$ are no longer simply displaced by a constant amount with respect to each other and therefore are no longer perfectly nested, the effect is not large.

As we have already discussed, the $-\epsilon_1 \rightarrow +\epsilon_2$ transitions remain unaffected by a finite but small value of μ and the onset for these transitions remains unshifted in energy at $E_{01} + E_{02} \simeq 1.1$. However, the optical weight at the onset is depleted because the $-\epsilon_2 \rightarrow +\epsilon_1$ transi-

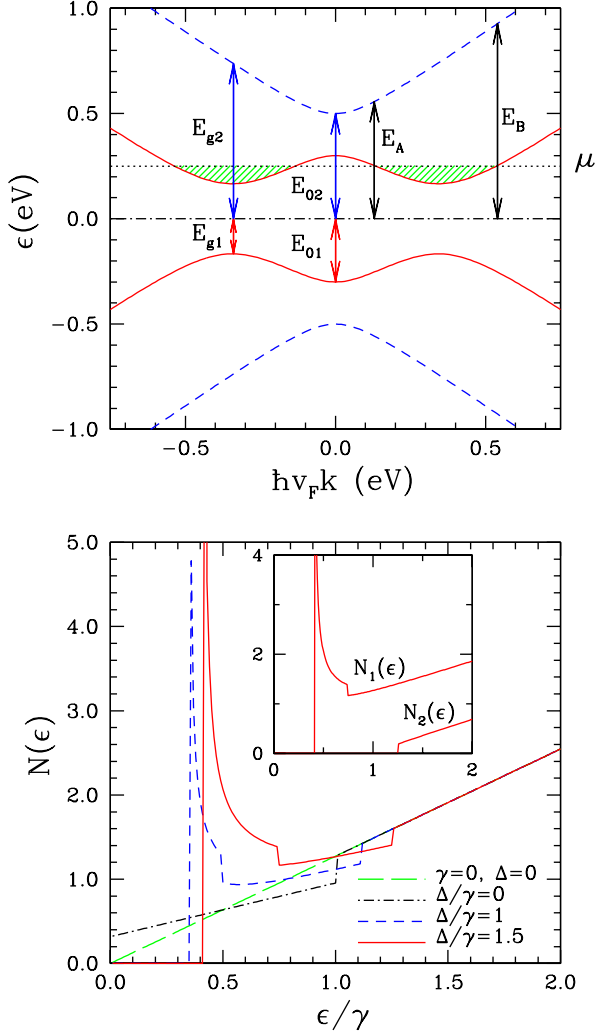


FIG. 5: (Color online) Top frame: Band structure around the Fermi level in the presence of the asymmetry gap Δ for realistic values of $\Delta = 0.6$ eV and $\gamma = 0.4$ eV. A finite chemical potential of $\mu = 0.25$ eV is shown. Various important energies are indicated in the figure and displayed in Table I. Bottom frame: The density of states $N(\epsilon)$, in units of $\gamma/\hbar^2 v_F^2$, for the bilayer for several values of Δ as indicated in the figure, in comparison with the case of $\gamma = \Delta = 0$ corresponding to the uncoupled graphene bilayer. The inset shows the partial density of states $N_1(\epsilon)$ and $N_2(\epsilon)$ for the two separate bands ϵ_1 and ϵ_2 , respectively, for the case of $\Delta/\gamma = 1.5$.

tions do know about μ . For $\mu = 0.1\gamma$, these transitions are blocked in the energy range $E_A + \mu = 1.115\gamma$ to $E_B + \mu = 1.134\gamma$. Both these energies fall very close to the peak energy 1.1γ and show up in the figure simply as a slight depletion of the large broad peak above $\Omega = 1.1\gamma$ in the dashed blue curve.

Similar arguments explain the main features seen in the solid red curve for $\mu = 0.2\gamma$. In this case, the cutoff imposed on the $-\epsilon_1 \rightarrow +\epsilon_1$ transitions is at $\Omega = 0.4\gamma$ (2μ) and the amount of spectral weight transferred to

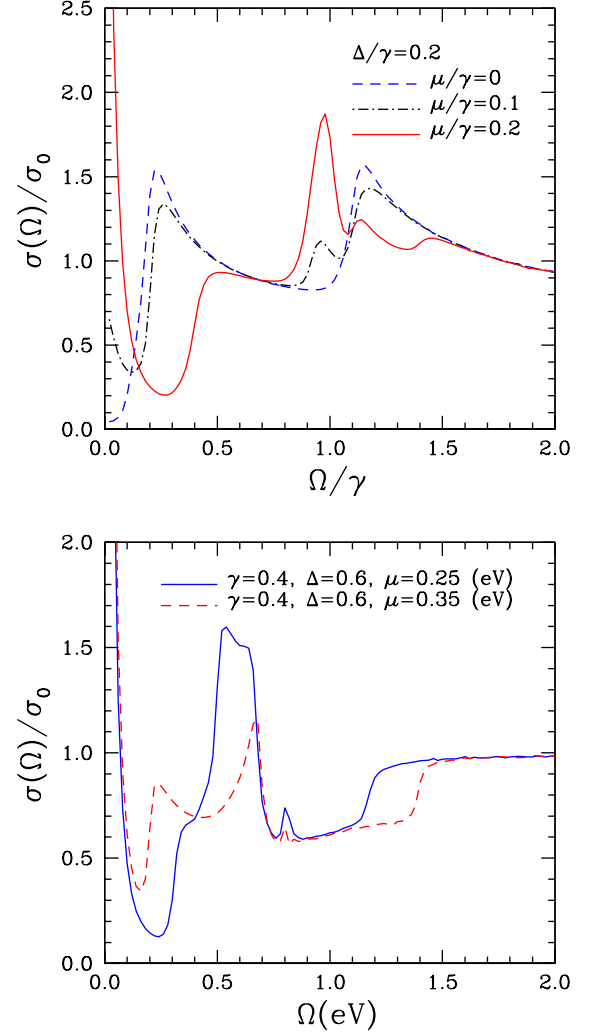


FIG. 6: (Color online) Optical conductivity in the presence of an asymmetry gap Δ . The upper frame shows the results for varying μ with fixed $\Delta = 0.2\gamma$. The bottom frame shows the result for realistic values of the parameters, i.e., $\Delta = 0.6$ eV and $\gamma = 0.4$ eV. Here two curves are shown, one for $\mu = 0.25$ eV where the chemical potential lies above the gap in the band structure but below the hat maximum, and $\mu = 0.35$ eV, where it lies above the hat maximum.

the Drude centered at $\Omega = 0$ has greatly increased as compared with the dash-dotted black curve. The peak from the new $+\epsilon_1 \rightarrow +\epsilon_2$ transitions has broadened extending from 0.9γ , set by $E_{02} - E_{01}$ (as μ is now above the hat maximum) to 0.998γ , set by $E_B - \mu$. Finally, the upper cutoff on the $-\epsilon_2 \rightarrow +\epsilon_1$ transitions has moved to $E_B + \mu = 1.4$ eV, where a sharp rise in conductivity is seen.

In a field effect device with a semiconducting gap, the value of Δ cannot be set independently from the value of the chemical potential μ which sets the occupation of the $+\epsilon_1$ band and E_{g1} , the energy of the minimum of the mexican hat. Realistic values based on numerical work

presented in Ref.²² are $\gamma = 0.4$, $\Delta = 0.6$, and $\mu = 0.35$. Results for the conductivity $\sigma(\Omega)/\sigma_0$ versus Ω are shown as the dashed red curve in the bottom frame of Fig. 6. We found it illuminating also to present for comparison the case of $\mu = 0.25$ represented by the solid blue curve. The band structure involved is shown in the top frame of Fig. 5, where various energies of importance for optical transitions are identified. Actual numbers for the E_i 's are found in Table I. All the important qualitative features seen in the conductivity curves can be understood on the basis of these energy scales. We begin with the solid blue curve. If the chemical potential was zero the $-\epsilon_1 \rightarrow +\epsilon_1$ transitions would start at $2E_{g1} = 0.333$ eV but for $\mu = 0.25$ these are cutoff at 0.5 eV where we see a sharp rise in conductivity. On the other hand, the $+\epsilon_1 \rightarrow +\epsilon_2$ transitions, made possible through the finite occupation of the $+\epsilon_1$ states at finite chemical potential μ , start at $E_A - \mu = 0.31$ eV where we see the first rise in $\sigma(\Omega)$ after the Drude. These transitions extend to $E_B - \mu = 0.67$ eV where the conductivity shows a steep drop. Thus, the nested transitions of the $\Delta = 0$ bilayer graphene case are now greatly broadened and their onset has moved below the onset for the $-\epsilon_1 \rightarrow +\epsilon_1$ transitions. The small peak at $E_{01} + E_{02} = 0.8$ eV is traced to the $-\epsilon_2 \rightarrow +\epsilon_1$ and $-\epsilon_1 \rightarrow +\epsilon_2$ transitions which, as we have discussed, are depleted by charging but their onset remains unshifted. Finally the rise at $E_B + \mu = 1.17$ eV coincides with the upper cutoff on the $-\epsilon_2 \rightarrow +\epsilon_1$ transitions. For $\mu = 0.35$ eV (dashed red curve) the $+\epsilon_1 \rightarrow +\epsilon_2$ transitions start at $E_{02} - E_{01} = 0.2$ eV and cause the first rise in conductivity which follows the Drude peak about $\Omega = 0$. They extend to up $E_B - \mu = 0.69$ eV where the conductivity shows a rapid decrease. We stress that the onset of these transitions is set by the difference $(E_{02} - E_{01})$ (bottom of second band minus top of mexican hat) and not directly by the chemical potential which falls above E_{01} . The peak at 0.8 eV is further depleted as compared with the solid blue curve but is unshifted. The upper cutoff on the $-\epsilon_2 \rightarrow +\epsilon_1$ transitions is now at $E_B + \mu = 1.39$ eV.

In Fig. 7, we show results for the partial optical sum $I(\Omega)$ in units of γ versus Ω/γ which describes the optical weight redistribution brought about by the opening of the anisotropy gap and finite chemical potential. Four cases are compared in the main frame for $\mu = 0$. The dash-dotted green curve is for $\Delta = 0$, long dashed black for $\Delta/\gamma = 0.5$, solid red for $\Delta/\gamma = 1.0$, and short dashed blue for $\Delta/\gamma = 1.5$. We see the almost complete depletion of optical spectral weight below the gap $2E_{g1}$ set by the minimum energy in the mexican hat dispersion curves. The small tails below this cutoff are due to the impurity smearing caused by our use of a finite $1/\tau_{imp}$ in the numerical work. In all cases, the lost spectral weight is recovered in the region above it. The overshoot beyond the reference curve (dash-dotted green) is largest for the largest Δ considered and in this case $I(\Omega)$ is still slightly above the $\Delta = 0$ reference even at $\Omega = 3$ eV. It is clear, however, that there is a close balance between

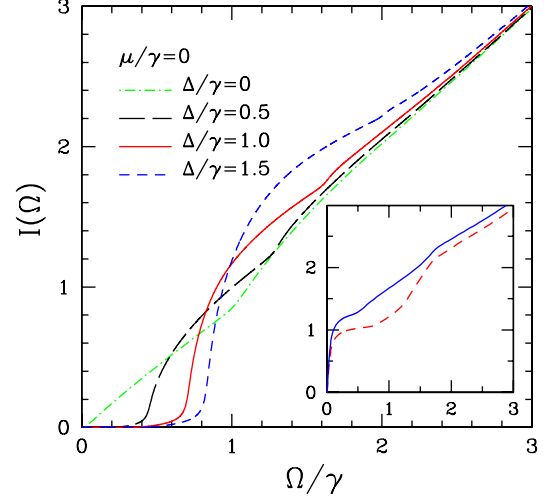


FIG. 7: (Color online) The partial optical sum $I(\Omega)$ in units of γ versus Ω/γ for various values of Δ with $\mu = 0$. Inset: $I(\Omega)$ for the more realistic parameters used for $\sigma(\Omega)$ in Fig. 6b, i.e., $\gamma = 0.4$ eV, $\Delta = 0.6$ eV, and $\mu = 0.25$ eV (dashed red curve) and 0.35 eV (solid blue curve).

weight lost and gained in this interval. In the inset of Fig. 7, we show $I(\Omega)$ in units of γ versus Ω/γ for more realistic values of γ , Δ , and μ associated with the conductivity curves shown in the bottom frame of Fig. 6. For μ finite, there is a narrow Drude peak in $\sigma(\Omega)$ with width set by $1/\tau_{imp}$, which results in a fast rise of $I(\Omega)$ out of $\Omega = 0$. This is followed by further rises with small kinks reflecting the sharp rises and drops in the associated conductivity curves.

V. SUMMARY AND DISCUSSION

We have derived an analytic algebraic formula for the zero temperature, clean limit optical conductivity of a graphene bilayer valid for any value of charge imbalance characterized by a general value of the chemical potential μ . In the limit of $\mu = 0$ our formula reduces properly to that of Abergel and Fal'ko¹⁸. A finite μ introduces several important modifications. First, some of the low energy $-\epsilon_1 \rightarrow +\epsilon_1$ transitions are no longer allowed because the charge imbalance leads to finite occupation of part of the $+\epsilon_1$ band. Furthermore, new $+\epsilon_1 \rightarrow +\epsilon_1$ intraband transitions are now possible and this leads to a finite Drude peak at $\Omega = 0$. In addition, new interband transitions between $+\epsilon_1 \rightarrow +\epsilon_2$ are allowed and these lead to a second delta function contribution at $\Omega = \gamma$. These transitions reflect the perfect nesting between bands 1 and 2 which are simply displaced in energy by a constant amount γ in our model band structure when there is no anisotropy gap. For more complicated models in which the nesting ceases to be perfect, the peak at $\Omega = \gamma$ would broaden into an absorption band whose width and struc-

ture in energy reflects the mismatch in topology between bands 1 and 2. In addition, there is a broadening brought about by the elastic scattering rate $1/\tau_{imp}$. Immediately above the $\Omega = \gamma$ peak there is a second depletion region which is due to the blocking of the $-\epsilon_2 \rightarrow +\epsilon_1$ transitions between γ and $\gamma + 2\mu$. The presence of a finite μ does not affect the $-\epsilon_1 \rightarrow +\epsilon_2$ transitions which also fall in the same energy interval and so only partial depletion is involved. It is found that the optical spectral weight lost in the two depletion regions is completely compensated for by the spectral weight which resides in the delta function. We have just described the case for $\mu < \gamma$. For $\mu > \gamma$, new intraband transitions associated with the $+\epsilon_2 \rightarrow +\epsilon_2$ transitions become possible and the transitions which utilize band 2 as the final state also become blocked.

Note that all the main features of the conductivity curves found here can be traced directly to the underlying band structure of bilayer graphene. Correlation effects, which have not been treated here, lead to self-energy (Σ) corrections. The real part of Σ renormalizes the single particle energies and the imaginary part introduces damping. Angle-resolved photoemission spectroscopy (ARPES) provides a direct measure of the dressed dispersion curves and of their many body broadening. The ARPES data^{5,28} confirms the general shape of the tight-binding dispersion curves used here with some smaller modification and by implication, we do not expect large changes in the frequency dependence of the conductivity described here. Of course, the scattering rate due to many body interactions will, in general, be frequency dependent while here we have treated it as a constant. In bilayer graphene, even impurity scattering involves an energy-dependent scattering rate and many examples of how this changes the shape of the optical conductivity can be found in the recent work by Nilsson et al.²⁶ Finally, we note that vertex corrections have not been included here as this goes beyond the present work.

When a semiconducting gap is introduced, the band structure becomes modified. In particular, band 1 acquires a mexican hat structure with the top of the hat at energy $E_{01} = \Delta/2$ and the minimum on the rim of the hat is at $E_{g1} = (\Delta\gamma/2)/\sqrt{\Delta^2 + \gamma^2}$. This can be achieved in a graphene bilayer when donor atoms are

seeded on its top surface and the whole is placed in a field effect configuration. In such junctions, finite Δ also implies finite $\mu > E_{g1}$ and there exists a finite charge imbalance. Only for the case of finite Δ and $\mu = 0$ is there a real gap in the system, i.e. no absorption below $2E_{g1}$: the $-\epsilon_1 \rightarrow +\epsilon_1$ transitions become gapped and the lost optical spectral weight is found to accumulate in the energy region just above the gap on an energy scale of order Δ . In any practical case, however, a finite value of chemical potential accompanies a finite Δ and there is a Drude centered at $\Omega = 0$ and a cutoff on the $-\epsilon_1 \rightarrow +\epsilon_1$ transition of 2μ . The onset of the $-\epsilon_1 \rightarrow +\epsilon_2$ (and $-\epsilon_2 \rightarrow +\epsilon_1$) moves from γ in the case of $\Delta = 0$ to $E_{01} + E_{02} = \sqrt{(\Delta/2)^2 + \gamma^2} + (\Delta/2)$. The $-\epsilon_2 \rightarrow +\epsilon_1$ transitions become gapped in the interval $E_A + \mu$ to $E_B + \mu$, unless $\mu > \Delta/2$, then the lower limit changes to $E_{01} + E_{02}$. In addition, the transitions from $+\epsilon_1 \rightarrow +\epsilon_2$, which are possible for finite μ and which in pure unbiased bilayer graphene provide a delta function at γ , are broadened into a band from $E_A - \mu$ to $E_B - \mu$, the width of which depends on the value of chemical potential. This band of absorption starts at energies below γ , with onset at the energy of the top of the mexican hat if μ is greater than this energy. While these modifications in the possible transitions due to finite Δ and μ can lead to complicated spectral weight shifts in $\sigma(\Omega)$ versus Ω , all changes can be understood qualitatively from a knowledge of the band structure involved. Biased graphene bilayers offer a rich pattern of variation of $\sigma(\Omega)$ versus Ω as the size of the anisotropy gap is varied through changes in the voltage of the field effect device. This system is not only important because of possible practical applications, but it is also the only system known for which the value of the semiconducting gap can be tuned by the application of an external voltage.

Acknowledgments

This work has been supported by NSERC of Canada and by the Canadian Institute for Advanced Research (CIFAR). J. P. C. thanks S. Sharapov and L. Benfatto for instructive discussions.

* Electronic address: nicol@physics.uoguelph.ca

¹ K. S. Novoselov, A. K. Geim, S. V. Morozov, D. Jiang, M. I. Katsnelson, I. V. Grigorieva, S. V. Dubonov, and A. A. Firsov, *Nature* **438**, 197 (2005).

² Y. Zhang, Y. W. Tan, H. L. Stormer, and P. Kim, *Nature* **438**, 201 (2005).

³ V. P. Gusynin and S. G. Sharapov, *Phys. Rev. Lett.* **95**, 146801 (2005).

⁴ N. M. R. Peres, F. Guinea, and A. H. Castro Neto, *Phys. Rev. B* **73**, 125411 (2006); A. H. Castro Neto, F. Guinea, and N. M. R. Peres, *Phys. Rev. B* **73**, 205408 (2006).

⁵ T. Ohta, A. Bostwick, T. Seyller, K. Horn, E. Rotenberg *Science* **313**, 951 (2006).

⁶ E. V. Castro, K. S. Novoselov, S. V. Morozov, N. M. R. Peres, J. M. B. Lopes dos Santos, J. Nilsson, F. Guinea, A. K. Geim, and A. H. Castro Neto, *Phys. Rev. Lett.* **99**, 216802 (2007).

⁷ E. McCann, *Phys. Rev. B* **74**, 161403(R) (2006).

⁸ E. McCann and V. I. Fal'ko, *Phys. Rev. Lett.* **96**, 086805 (2006).

⁹ J. Nilsson, A. H. Castro Neto, F. Guinea, and N. M. R. Peres, *Phys. Rev. Lett.* **97**, 266801 (2006).

- ¹⁰ A. K. Geim and K. S. Novoselov, *Nature Materials* **6**, 183 (2007).
- ¹¹ A. H. Castro Neto, F. Guinea, N. M. R. Peres, K. S. Novoselov, and A. K. Geim, arXiv:0709.1163.
- ¹² M. L. Sadowski, G. Martinez, M. Potemski, C. Berger, and W. A. de Heer, *Phys. Rev. Lett.* **97**, 266405 (2006).
- ¹³ M. L. Sadowski, G. Martinez, M. Potemski, C. Berger, and W. A. de Heer, *Solid State Comm.* **143**, 123 (2007).
- ¹⁴ Z. Q. Li, S. W. Tsai, W. J. Padilla, S. V. Dordevic, K. S. Burch, Y. J. Wang, and D. N. Basov, *Phys. Rev. B* **74**, 195404 (2006).
- ¹⁵ A. B. Kuzmenko, E. van Heumen, F. Carbone, and D. van der Marel, arXiv:0712.0835.
- ¹⁶ Z. Jiang, E. A. Henriksen, L. C. Tung, Y.-J. Wang, M. E. Schwartz, M. Y. Han, P. Kim, and H. L. Stormer, *Phys. Rev. Lett.* **98**, 197403 (2007).
- ¹⁷ T. Ando, Y. Zheng and H. Suzaura, *J. Phys. Soc. of Japan* **71**, 1318 (2002).
- ¹⁸ D. S. L. Abergel and V. I. Fal'ko, *Phys. Rev. B* **75**, 155430 (2007).
- ¹⁹ L. A. Falkovsky and A. A. Varlamov, *Euro. Phys. J. B* **56**, 281 (2007).
- ²⁰ V. P. Gusynin, S. G. Sharapov and J. P. Carbotte, *J. Phys.: Condens. Matter* **19**, 026222 (2007).
- ²¹ V. P. Gusynin, S. G. Sharapov and J. P. Carbotte, *Phys. Rev. B* **75**, 165407 (2007).
- ²² L. Benfatto, S. G. Sharapov and J. P. Carbotte, arXiv:0712.1885.
- ²³ J. P. Carbotte and E. Schachinger, *J. Low Temp. Phys.* **144**, 61 (2006).
- ²⁴ V. P. Gusynin, S. G. Sharapov and J. P. Carbotte, *Phys. Rev. Lett.* **96**, 256802 (2006).
- ²⁵ G. D. Mahan, *Many-Particle Physics*, Plenum, New York (1990).
- ²⁶ J. Nilsson, A. H. Castro Neto, F. Guinea and N. M. R. Peres, arXiv:0712.3259
- ²⁷ G. P. Mikitik and Yu. V. Sharlai, arXiv:0709.1803
- ²⁸ A. Bostwick, T. Ohta, T. Seyller, K. Horn and E. Rotenberg, *Nature Physics* **3**, 36 (2007).